Journal of Hazardous Materials Advances 21 (2026) 101055

Contents lists available at ScienceDirect

Journal of Hazardous Materials Advances

journal homepage: www.elsevier.com/locate/hazadv

Implementation of a multidisciplinary radon risk assessment of building materials in existing scenario in Sant'Agata de'Goti

Fabrizio Ambrosino [a,b], Manuela Rossi [c,*], Andrea D'Elia [a], Chiara Imparato [d], Mariagabriella Pugliese [a,b,1], Giuseppe La Verde [a,b,*,1]

[a] Dipartimento di Fisica "Ettore Pancini", Università degli Studi di Napoli Federico II, Via Cinthia ed. 6, 80126 Napoli, Italy
[b] Istituto Nazionale di Fisica Nucleare, INFN sezione di Napoli Via Cinthia ed. 6, 80126 Napoli, Italy
[c] Dipartimento di Scienze della Terra, dell'ambiente e delle Risorse, Università degli Studi di Napoli Federico II, Via Cinthia ed. 10, 80126 Napoli, Italy
[d] Dipartimento di Matematica e Fisica, Università degli Studi della Campania Luigi Vanvitelli, Viale Abramo Lincoln n. 5, 81100 Caserta, Italy

ARTICLE INFO

Keywords:
Indoor radon
Building materials
Campanian ignimbrite
Exhalation rate
Gamma spectrometry
Electret ion chamber
Zeolites
Volcanic tuff
Italy
Risk assessment

ABSTRACT

Radon exposure is still a significant public health concern, particularly in regions where natural building materials are derived from high-radiation subsoils. This study proposes a multidisciplinary protocol for assessing radon risk in existing buildings, with a specific focus on the municipality of Sant'Agata de' Goti (southern Italy), a historical town built entirely of Campanian Ignimbrite tuff. Indoor radon concentrations were monitored using CR-39 detectors in 20 locations over a one-year period, revealing that 70 % of the measured values exceeded the regulatory threshold of 300 Bq/m^3. Complementary analyses were conducted on tuff samples used as Building Materials (BMs), including gamma spectrometry, electret ion chamber, X-ray fluorescence (XRF), and scanning electron microscopy with energy-dispersive spectroscopy (SEM-EDS) measurements. High levels of Ra-226 and Th-232, along with elevated exhalation and emanation parameters, were observed. The study highlights how petrographic and mineralogical features - such as pumice porosity, zeolitization, and microstructure - enhance radon release beyond what is predicted by radionuclide content alone. The *I* index exceeded unity in both analyzed facies - the yellow one and the gray one of the Ignimbrite tuff - suggesting these materials pose a radiological hazard. The results highlight the need to integrate BMs characterization into National Radon Action Plans, particularly in areas with widespread historical use of volcanic tuff. This would include BMs already in use and not just those in pre-commercialization, as is required by current regulations. The proposed approach provides a replicable model for assessing radon risk in existing structures and supports targeted mitigation strategies based on multidisciplinary data.

1. Introduction

Exposure to ionizing radiation from both natural and artificial sources is an inherent part of life on Earth and a well-documented health risk (National Research Council 2006; UNSCEAR 2000). Natural radioactivity is the primary component of environmental background radiation, with radon being the largest contributor, accounting for about 50 % (UNSCEAR 2008). Among the radioisotopes, of particular interest are: radon-222 (Rn-222), which derives from the decay chain of uranium-238 (U-238), has the longest half-life (3.82 days) and contributes 31.6 % to background radiation; and thoron (Rn-220), derived from thorium-232 (Th-232), with a half-life of 55.6 s, contributing 10 %. However, due to its relevance and abundance in the environment, Rn-222 is the only one conventionally considered.

Rn-222, the decay product of radium (Ra-226), is an inert gas and, due to its gaseous nature, can escape from the mineral structure and enter the rock pores. This process is known as emanation and constitutes the fraction that is potentially available for release into the external environment (exhalation process). The specific position of the decaying radionuclide and the recoil direction of the newly formed radon atom significantly influence emanation. Physical factors, including humidity, temperature, the distribution of radionuclides within the mineral structure, and pore characteristics, influence the emanation/exhalation process. (Sakoda et al., 2010). In fact, Rn can reach the atmosphere

* Corresponding authors.
E-mail addresses: manuela.rossi@unina.it (M. Rossi), giuseppe.laverde@unina.it (G. La Verde).
[1] These authors contributed equally to this work.

https://doi.org/10.1016/j.hazadv.2026.101055
Received 18 September 2025; Received in revised form 22 January 2026; Accepted 3 February 2026
Available online 17 February 2026

depending on the matrix permeability, thus accumulating in closed environments. In addition to the aspects specifically related to the matrix, other main routes of entry and accumulation of radon gas indoor are cracks in foundations, walls and pipes, water systems (showers and taps), and building materials (BMs) (UNSCEAR 2008; Di Carlo et al., 2023) Inhalation of Rn-222 poses a significant health risk [(Pawel and Puskin, 2004; World Health Organization (WHO) 2009; International Agency for Research on Cancer (IARC) 2012)]. The primary health risks associated with Rn-222 exposure, rather than from the gas itself, arise from its short-lived radioactive decay products, polonium 218 and 214 (Po-218 and Po-214) (UNSCEAR. Sources 2012). Alpha decay from these isotopes can damage DNA, leading to mutations and an increased risk of lung cancer. Studies have shown a correlation of 3–14 % between lung cancer incidence and radon exposure [(International Commission on Radiological Protection (ICRP) 2014; Liu et al., 2024; Darby et al., 2005)]. Due to the associated health risks, international and national regulations (Decreto Legislativo 31 luglio 2020; Council Directive 2013/59/Euratom of 5 December 2013 2014) mandate the consideration of all potential radon sources, including BM. Over the years, the Italian government has adopted various Legislative Decrees (D.L.) for monitoring radon gas in buildings. In 2000, D.L. 241/2000 (Decreto Legislativo 26 maggio 2000, n. 241 2000) identified workplaces on ground floors and thermal baths as the scope of application. In 2020, D. L. 101/2020, implementing the European Directive Euratom 59/2013, introduced the principle of optimization in radiation protection through a gradual approach, extending the scope to dwellings. Furthermore, in compliance with the Directive (Article 103 and Annex XVIII), and similarly to other European countries, D.L. 101/2020 introduced a National Radon Action Plan (NRAP) (Ministero della Salute 2024) highlighting the need for a specific plan to measure and monitor indoor radon (Silva et al., 2022).

Within the regulatory framework, BMs are only monitored to assess

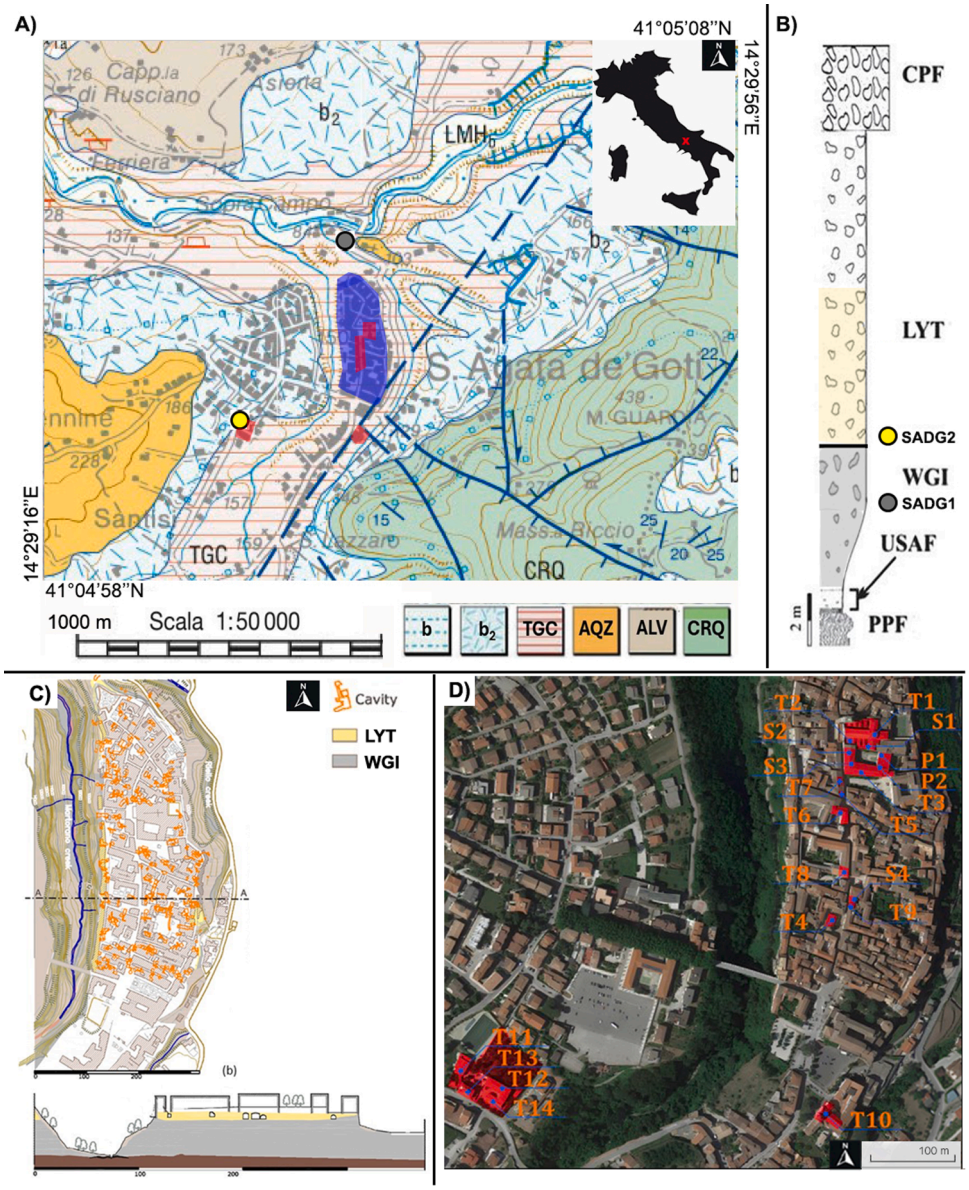

Fig. 1. A) Areas where the sampling was conducted (samples with radiometric anomalies). In yellow, sample SADG2; in grey, sample SADG2. *b* = alluvial deposits, b2 = eluvial and colluvial covers, TGC = Campanian grey tuff (ignimbrite), AQZ = Campoli sandstones, ALV = varicolored clays, CRQ = limestones with requienia and gastropods ((Monti et al., 2011), (Carannante et al., 2011) modified; B) Stratigraphic column of the Campanian Ignimbrite (from (Cappelletti et al., 2003) - modified); C) Map of the 160 underground cavities in Sant'Agata de' Goti. (b) Stratigraphic section of the historic center of Sant'Agata de' Goti (from (Scotto di Santolo et al., 2014) –modified); D) Map of the CR39 detectors' positioning in places from Google Earth™ Pro (modified), at different heights above the ground: S (basement), T (ground floor), P (first floor).

radiometric suitability for marketing and ensure compliance with the standards of European regulation no 305/2011 (European Union 2011), excluding existing exposure scenarios from risk management. Regarding the NRAP, while the main objective is to identify high-risk radon areas and start actions to reduce exposure (Hodgson et al., 2011), there is also a need for radiological identification and characterization of BMs considering the radon exhalation rate (Action 2.3 NRAP).

This aspect requires the definition of shared and standardized experimental protocols to comply with the aforementioned requirement, which are still being defined today (Martell et al., 2023).

This work therefore addresses a current issue with seemingly few solutions, proposing, with experimental measures, an approach that can integrate regulatory requirements and good practices, aimed at guaranteeing the maximum radiation protection possible.

The aim was to report a case study of existing exposure in a village entirely built on a volcanic tuff spur, Sant'Agata de' Goti (in Campania, southern Italy), which had been preliminarily investigated (La Verde et al., 2020). The implications are twofold: to highlight the need to consider existing exposure scenarios not covered by the legislation and to validate a multidisciplinary approach to radiometric characterization.

This methodological approach included: indoor radon measurements; measurements of gamma-emitting radionuclides, implementing a preliminary investigation (Pugliese et al., 2024); radon exhalation and emanation measurements; and chemical and morphological analyses. The results are promising for developing standardized operational protocols for holistic radon risk management.

2. Materials and methods

2.1. Studied area: Sant'Agata de' Goti

The study was carried out in the urban area of Sant'Agata de' Goti, a village of Roman foundation in Campania (southern Italy),in the province of Benevento, on the western slopes of Mount Taburno (Fig. 1A). Two sampling sites were selected, for two lithotypes, similar to those used in the construction of the historic buildings (samples SADG1 and SADG2). The first, SADG1, near the area of Sopracampo, and the second, SADG2, in the town center of Sant'Agata dei Goti, between Viale dei Caduti and Viale Picone. From a lithographic point of view, they correspond to two different typologies of Campanian Grey Tuff: grey (SADG1) and yellow (SADG2) facies (Fig.1B). Three tuff samples were taken for each sampling point. This number, although limited due to landscape and land preservation constraints, is sufficient and representative of the two types of BMs. The primary information on the collected tuff samples and the geology of Sant'Agata de' Goti is extracted from the explanatory notes of the Geological Map of Italy, Sheet 432 Benevento (Monti et al., 2011) and Sheet 431 Caserta Est [(Chiocchini et al., 2009); Fig. 1A]. The tuff on which the village stands and with which it is built can be classified as Campanian Grey Tuff, produced by the eruption of the Campanian Ignimbrite (De Vivo et al., 2001). 40-Ar/39-Ar analyses on Campanian Ignimbrite date the origin of the first eruptive phase to 39.28±0.11 ka years ago (De Vivo et al., 2001). The fall deposit that constitutes the base of the Campanian Grey Tuff is composed of alkaline trachyphonolitic pumices (Di Girolamo et al., 1973). From the lowest to the highest level, both the presence and the size of dark pumices increase while lava and sedimentary fragments decrease. The superficial ignimbrite portion, and therefore the most exposed one, can take on a yellowish color. This yellow facies, not to be confused with the Neapolitan Yellow Tuff originated from an eruption 15,000 years ago, owes its color and more coherent consistency to the effect of a secondary lithification process, in most cases a zeolitization (Cappelletti et al., 2003). Fig. 1B shows the stratigraphic column of the Campanian Ignimbrite at Sant'Agata de' Goti village and below is a detailed description:

Coarse Pumice Flow (CPF) – The uppermost portion of the Campanian Ignimbrite is an incoherent unit composed of rounded pumice lapilli and clasts within abundant loose glass shards.

Lithified Yellow Tuff (LYT) – This locally occurring unit is a massive and lithified yellow ash deposit. It consists of an ash matrix with dispersed rounded pumice lapilli. Occasionally, a few coarse scoria fragments can be found. It rests on the WGI.

Welded Grey Ignimbrite (WGI) – A significant part of the Campanian Ignimbrite deposit consists of a grey ash layer ranging from a few meters to several tens of meters in thickness. The lower massive part (several centimeters thick) is white to cream-colored, relatively fine-grained, and contains scattered pumice lapilli and rare scoria lapilli towards the upper section. This lower part gradually darkens and transitions upwards into a welded grey zone containing rounded scoria lapilli. This welded grey horizon is the most widespread facies associated with the Campanian Ignimbrite (previously known as Grey Tuff). It consists of black scoriae, reverse graded, embedded in an ashy matrix with subordinate lithics and crystals.

Unconsolidated Stratified Ash Flow (USAF) – This is a stratified and incoherent ash to sandy deposit, with colors ranging from whitish at the base to reddish at the top. Its thickness varies from a few centimeters to a maximum of about 50 cm. This unit contains scattered varying amounts of fine, rounded pumice lapilli. A laterally discontinuous level of the USAF is characterized by abundant lithics and crystals.

Plinian Pumice Fall (PPF) – The entire deposit is represented by four main layers, from A to D, from bottom to top, composed of pumice lapilli ranging in size from coarse to fine, along with smaller amounts of lithic clasts and crystals, except for layer C, which shows a marked enrichment in lithics and crystals. This sequence is capped by a thin stratified lapilli level that is sandy to fine-grained at the uppermost part (E); this layer is often eroded and directly underlies the ignimbritic succession.

The entire village is divided into two parts: a modern one, built starting from the late 19th century, and the other of Roman foundation, located on a tuff cliff and characterized by approximately 160 underground cavities (Fig. 1.C). These are the result of an ancient technique of quarrying tuff bricks, which were then used to construct the buildings above (Artiola et al., 2021; La Verde et al., 2021). Most of the village's houses rest directly on the tuff layer (LYT) and are built with tuff bricks extracted from the underlying layer of Campanian Ignimbrite.

This particular conformation makes the investigation of the distribution and concentration of indoor radon gas in these buildings even more interesting. Therefore, a survey was conducted by selecting the number of buildings in accordance with the NARP guidelines, which establish that the minimum number of measurement points, y, necessary to identify priority areas for radon risk can be calculated using the formula $y = x\hat{}0.3$, where x is the number of inhabitants. For a municipality like Sant'Agata de' Goti with 10,000 inhabitants (ISTAT 2025) the minimum number of buildings is 16. So, a total of 20 buildings were selected, 16 of which were located along the main and oldest artery of the village, built with tuff extracted from subsoil, and 4 in a newer building complex southwest of the town, including reinforced concrete structures, as shown in Fig. 1.D.

Although the intended use is not that of a living environment (ecclesiastical premises, shops, caves), the rooms are all exactly comparable to domestic environments.

2.2. CR-39 for indoor radon survey

Passive CR-39 Solid-State Nuclear Track Detectors (SSNTDs) made of a plastic polymer called polyallyl diglycol carbonate were used for the survey. The detector is inserted into a conductive plastic chamber, which allows the radon to diffuse naturally within it. Once the radon gas decays inside the chamber, the alpha particles produced interact with the sensing material, damaging its chemical bonds and producing latent tracks (more details are reported in (Fews and Henshaw, 1982)). These tracks are made visible through chemical etching in a 6.25 M NaOH solution at 98 ± 1 °C for one hour, according to UNI ISO 11665-4: 2020 (UNI ISO 11665-4:2020 2020).

Subsequently, an automated microscopic image analyzer counted the track density (Sabbarese et al., 2020). Radon concentration (Rn_{con}) was calculated using the following Eq. (1):

$$Rn_{con} = N / (E \times T) \quad (1)$$

Where:

N is the track density corrected for background,

E is the calibration factor,

T is the exposure time.

The background track density was estimated at 10 tracks/cm^2 based on unexposed detector counts. The measured track densities were converted into radon concentration by using the following calibration factor 0.00209 ± 0.00021 tracks·cm^2·h^{-1}/Bq·m^3., determined through exposure to a certified atmosphere at the National Metrological Institute (ENEA) within the 100 to 3000 Bq h m^3 range. The Minimum Detectable Activity (MDA) was estimated at 4 Bq/m^3 with a 4320-hour exposure.

The CR39 were positioned inside the rooms at a height of approximately 2 m from the ground and at least 0.5 m away from the surrounding walls to avoid the interference of thoron. Measurements were carried out for approximately one year, divided into two semesters: from 18/07/23 to 20/11/23 (the first semester), and from 20/11/23 to 31/05/24 (second semester).

2.3. Sample preparation for radiometric investigation

For each tuff sample, measurements were carried out both on the sample in its natural rock state (a cylinder approximately 8 cm in diameter and 1 cm high, same geometry as calibration source (Ambrosino et al., 2024)) and in a powdered form. To ensure a consistent and stable matrix, sample preparation followed the methodology outlined in UNI EN ISO 18589–2:2015 (UNI EN ISO 18589-2:2015 2015). The rock cylinders were sealed in Marinelli beakers to prevent radon leakage prior to gamma spectrometry measurements, and to ensure the secular equilibrium between Rn-222 and Ra-226. ANGLE software of Ortec company were used to evaluate the detector efficiency with different geometries To obtain the other type of sample, instead, bricks were ground into powder, sieved, and dried in an oven at 105 °C for two hours. The powdered samples were then homogenized and weighed before being placed in Marinelli Beaker containers for four weeks to achieve secular equilibrium between Ra-226 and Rn-222. Both types of samples were used for gamma spectroscopy and exhalation measurements.

2.4. Gamma spectroscopy

A coaxial High Purity Germanium (HPGe ORTEC®) detector (model GMX-45P4ST) was used for high-resolution gamma spectrometry. The detector's specific characteristics were detailed in (Artiola et al., 2021). The detector is characterized by an energy resolution quantified by a Full Width at Half Maximum (FWHM) of 2.16 keV at 1.33 MeV, coupled with a relative efficiency of 48 %. The minimum detectable activity (MDA) calculated by the system has a 95 % confidence level (Currie, 1968). Spectral data were acquired using the Ortec DSPEC-LF unit coupled with the MCA Emulator software, Maestro-32. Subsequent analysis was performed using GammaVision Spectrum Analysis Software, version 7.01. Counting times were set to 172,800 s (48 h) for samples and 259,200 s (72 h) for background, used for peak correction. A library of spectral lines for the major natural radionuclides, was used to analyze the spectra. The photopeaks used to determine the activity concentrations of Th-232 were the lines at 727.3 keV, 860.6 keV and 911.2 keV of its daughters Bi-212, Tl-208 and Ac-228 respectively. The photopeaks used to determine the activity concentrations of Ra-226 were the lines at 295.2 keV plus 351.9 keV and 609.3 keV plus 1120.4 keV of its daughters Pb-214 and Bi-214 respectively. Final values of the activities concentrations of Th-232 and of Ra-226 where calculated with a weighted average of the values obtained from the respective descendants. The photopeak used to determine the activity concentrations of K-40 was the line at 1460.5 keV. For sample analysis, the 205.32 keV and 202.12 keV lines were excluded, and the 143.76 keV line for U-235 was included to avoid interference from other radionuclides. A 1 L Marinelli beaker of liquid and sealed mixed nuclides standard source (Eckert & Ziegler Nuclitec GmbH) with an activity of 49 kBq, an energy range of 60–1836 keV, a density of 1 g/cm^3, and a resolution of 3 % was used for energy calibration and efficiency determination. Other specific references are: MIX31520BD, type QCRB1244, serial n. BG-4358, drawing Vz-1520–001, calibration standard NG3–251. ANGLE software of Ortec company were used to evaluate the detector efficiency with different geometries and also for different matrix compositions in order to correctly evaluate the self-absorption effects (particularly for low-energy gamma photons Standard uncertainty was calculated according to the UNI EN ISO 18589-2:2015 (UNI EN ISO 18589-2:2015 2015).

2.5. INDEX I

The Index *I* (*I*), introduced by RP 112 of 1999 (Commission, 2002) and then adopted at European and Italian level, is a screening tool generally used to carry out assessments of suitability for marketing and use of BMs. *I* is defined by the following Eq. (2):

$$I = \frac{C_{Ra}}{300\ Bq/kg} + \frac{C_{Th}}{200\ Bq/kg} + \frac{C_K}{3000\ Bq/kg} \quad (2)$$

In Eq. (2), $C_{Ra\text{-}226}$, $C_{Th\text{-}232}$, and $C_{K\text{-}40}$ represent the activity concentrations of the corresponding radionuclides in the BMs, measured in Bq/kg. Further details regarding the parameter values of 300, 200, and 3000 can be found in reference (Markkanen, 1995). If *I* value is less than or equal to 1 ($I \leq 1$), the material is considered suitable for unrestricted use. However, if *I* value exceeds 1 ($I > 1$), a more precise calculation of the gamma dose (*D*) is necessary. If the calculated dose exceeds the reference level of 1 mSv/year, the material is deemed unsuitable for use in civil engineering structures, particularly residential and high-occupancy buildings.

2.6. Exhalation: sample surface area measurement

The lack of a standardized approach to expressing exhalation and emanation parameters is evident in both national and international literature (Sakoda et al., 2010; Ambrosino et al., 2024). These parameters are often reported using a variety of metrics, including the emanation coefficient (as a percentage), surface exhalation rate (Bq/(m^2·d)), and mass exhalation rate (Bq/(m^2·d)). This multiplicity of approaches makes it difficult to perform a meta-analysis. However, to convert from one unit to another, only information regarding the surface, volume, mass, and sample density is needed (Nuccetelli et al., 2020). In this work, therefore, the most commonly used exhalation parameters and the physical and geometric parameters necessary for any conversions are examined. In particular, a new protocol for measuring the emanation surface of irregularly shaped samples has been developed. For porous and friable BMs such as tuff, in fact, it can be difficult to obtain samples with a perfectly regular shape and without macro-porosity, essential when calculating their volume and surface area using geometric formulas.

ImageJ software (NIH, Bethesda, MD, USA) was used for image analysis. The sample preparation steps before acquisition are reported below:

1) Cover the sample with heat-shrinkable plastic and heat with a hot air gun until the plastic completely adheres to the irregular shape and macro-porosity of the sample.
2) Cover the plastic layer with a thin masking tape to create a thin shell that maintains the sample shape.

3) Extract the sample from the plastic and paper casing using a box cutter. Make deliberate cuts to the casing to create a two-dimensional image of the sample's surface without compromising its integrity.
4) Capture an image of the flattened shell, placed adjacent to a ruler for scale.
5) Open the image in ImageJ; use the pointer to select the longest visible distance on the ruler in the photo, then go to the Analyze menu, select "Set Scale" and enter the measurement in cm as indicated by the ruler so that the software can convert pixels to cm.
6) Go to Image > Adjust > Color Threshold to highlight the edges of the surface. Then, use the wand tracing tool to select the exact contours of the surface.
7) Select Image > Adjust > Color Threshold to enhance the surface edges. Finally, use the wand tracing tool to accurately select the surface boundaries.
8) Select Analyze > Measure to obtain the surface area measurement in cm^2.

2.7. Exhalation: electrets ion chamber

NRAP outlines the 'identification of BMs with higher radon exhalation' as a key action (Ministero della Salute 2024). While the plan does not prescribe a specific protocol, it encourages the exploration of the most appropriate method for measuring radon exhalation parameters. The most recent ISO standards regarding the measurement of radon exhalation parameters are the ISO 11665-7:2012 standard and the ISO 11665-9:2019 standard (UNI EN ISO 11665-7:2015 2012, UNI ISO 11665-9:2019 2019). The first one concerns the measurement of the Rn-222 surface exhalation rate (expressed in Bq/(m^2·h) over a short period of a few hours, at the interface of a medium with the atmosphere (soil or rock but can be extended to samples of BMs in general) and presents the difficulty of having an active monitor and a perfect airtight seal. The second method concerns the 'free exhalation rate' measurement (expressed in Bq/s) from samples of BMs, placed inside an accumulation chamber using passive detectors (activated carbon or silica gel) and requires sophisticated and expensive techniques such as Liquid Scintillation Counting (LSC) or gamma spectrometry (Nuccetelli et al., 2020; Poffijn et al., 1984; de Jong et al., 2005). For these reasons, the electret ion chamber has been considered among the most user-friendly instruments for measuring the emanation/exhalation parameters of the Sant'Agata tuff. This device is readily available and relatively affordable, with its effectiveness supported by numerous studies (Moreno et al., 2024; Kotrappa and Stieff, 2009; Righi and Bruzzi, 2006; Petropoulos et al., 2001). To measure the exhalation parameters, the tuff samples were placed at the bottom of an airtight jar with a volume of 3.843 L (Kotrappa and Stieff, 1994). Rock samples were mounted on small plastic pedestals to allow exhalation from their entire surface, while powdered samples were placed in metal cups to limit exhalation to the container's surface. At the top of the jar, connected to the inner part of the airtight cap, an E-PERM electret was connected in the short-term configuration (St electret and S chamber). Electret consists of an electrostatically charged Teflon plate with two different sensitivities (long and short term) attached to a diffusion chamber, also available in two configurations (long and short term). Air enters by passive diffusion in the chamber and, once equilibrium is reached, radon and its daughters decays by ionizing the air. The ions produced interact with the plate, discharging its surface voltage. The voltage difference allows the calculation of the radon activity concentration. More details are reported in (Rad Elec Inc 2024). Detectors were calibrated by participating in an international intercomparison (IRPA/AIRP 2024) where they were exposed to different of known radon activity concentrations and in constant environmental conditions (16.8 ÷ 30.5 °C, 965 ÷ 1008 mbar, and 2 humidity levels: 33.8 % ÷ 58.7 and 69.0 % ÷ 84.5).

To minimize relative error in activity concentration values and to prevent the negative impacts of back diffusion, which become significant after 6 days, a measurement period of 5 days was selected (Chao and Tung, 1999). A sample volume 10 times smaller than the jar's free volume is also sufficient to avoid the negative impacts of back diffusion (Krisiuk et al., 1971).

The exhalation rate can be derived from the measured activity concentration within the jar, C_{Rn} (Bq/m^3)by applying the following Formula (3):

$$R(\mathrm{Bq}/\mathrm{d}) = \frac{(C_{Rn} - C_{Rn0})\cdot V\cdot 0.1814}{K} \quad (3)$$

Where:

C_{Rn}= Average integrated activity concentration over exposure time (Bq/m^3)
C_{Rn0}= Average integrated background activity concentration (Bq/m^3)
V= volume of air in the chamber (m^3)0.1814 = decay constant of radon (1/d)

$$K = 1 - \left(\frac{1 - e^{-0.1814\ T}}{0.1814\ T}\right)$$

T= time of exposure (d).

Radon flux, F (Bq/(m^2·d)), was calculated applying the Formula (4):

$$F = \frac{R}{S} \quad (4)$$

Where S = sample surface (m^{-2}).

The mass exhalation rate, R_m, (Bq/(k·d) can be calculated applying the Formula (5):

$$R_m = \frac{R}{m} \quad (5)$$

Where m is the sample mass.

The emanation coefficient, η, (%) can be calculated applying the Formula (6):

$$\eta = \frac{R_m\cdot 100}{C_{Ra}\cdot 0.1814} \quad (6)$$

Where C_{Ra} is the activity concentration of ^{226}Ra of the sample measured with gamma spectroscopy.

2.8. Petrographic microscope

The petrographic microscope used is the AXIO IMAGER A1m by Zeiss powered by the Museum Center of Natural and Physical Sciences of University Federico II. The AxioCam ICc5 camera was used for image acquisition. The software used for image acquisitions is Axiovision SE64 Ref 4.9.1. Petrographic observations were carried out on two thin sections for each sample, obtained from different portions of rock collected at the two sampling sites, SADG1 and SADG2. Thin sections were examined to characterize not only the mineralogical composition of the samples but also their microstructural attributes, such as primary porosity, vesicles, and microfractures.

2.9. Scanning electron microscope - energy dispersive X-Ray spectroscopy (SEM-EDS)

Qualitative chemical analyses of the major and minor elements and detailed morphological characterization and qualitative chemical analyses were performed by using a scanning electron microscope (SEM) JEOL-JSM 5310, coupled with energy dispersive X-ray spectroscopy (EDS), at the DiSTAR laboratories. The setup is equipped with an Oxford Instruments Microanalysis unit, INCA X-act detector, operating at 15 kV primary beam voltage, 50–100 mA filament current, variable spot size,

20 mm WD, and 40 s net acquisition real time. INCA X-act detector uses Energy software with XPP matrix correction scheme and Pulse Pile up correction. Detailed morphological observations and qualitative chemical analyses were carried out on two fragments for each sample, obtained from different portions of rock collected at the two sampling sites, SADG1 and SADG2. The analyzed samples were coated with Au.

2.10. X-Ray fluorescence (XRF)

Chemical analyses of bulk-rock powder samples SADG1 and SADG2 were performed by X-ray fluorescence (XRF) using an Axios Panalytical sequential wavelength-dispersive spectrometer, equipped with a Rhodium (Rh) X-ray tube, six analyzing crystals (LiF220, LiF200, LiF420, PE002, PX1, TlAP), three collimators (150 μm, 550 μm, and 700 μm), four filters (Al 200 μm, Al 750 μm, Brass 100 μm, Brass 400 μm), and two detectors (a gas-flow counter and a scintillation detector), at the DiSTAR laboratories. Calibration was performed using 45 certified reference materials (Jochum and Enzweiler, 2014), and data acquisition was carried out with the SuperQ software. Analytical uncertainties are approximately 1–2 % for major elements and 5–10 % for trace elements. For XRF analyses, powder samples were prepared as pressed pellets. Loss on Ignition (L.O.I.) was determined by first drying the samples overnight at 105 °C to remove adsorbed moisture (H_2O^-), followed by calcination in a furnace at 1050 °C for approximately 4 h.

2.11. Mercury intrusion porosimetry

Mercury Intrusion Porosimetry (MIP) tests were performed using a Thermo Finnigan Pascal Hg porosimeter equipped with 140 and 440 devices. The first one applies low mercury pressure up to 400 kPa to introduce mercury into the sample and measure macroporosity. The second one applies a maximum pressure of 400 MPa for mesoporosity measurement, corresponding to a minimum measurable pore diameter of about 0.003 μm (ISO 15901-1:2016 (ISO 15901-1 2016)). Small but representative fragments (bulky volumes ≈1cm3), were selected, avoiding any changes in the natural distribution of the porous space. The samples were then dried for 24 h in a vacuum oven at ~70 °C before being analysed. Data were processed by SOL.I·D (Solver of Intrusion Data), software (Ver. 1.6.6. – Thermo Scientific), allowing to determine apparent and bulk densities, Hg-open porosity, total pore-surface area, and average, and modal pore diameter. Three measurements were the minimum number of average data for pore-size distribution curve (Fig 1S).

3. Results and discussion

3.1. Results: CR-39 survey

The results of the indoor radon activity concentration measurement campaign confirmed the high values hypothesized based on the available geo-lithological information about the village of Sant'Agata de' Goti. Table 1 shows the results for the two exposure periods. The first period, from 18/07/23 to 20/11/23, encompasses the warmer months, while the second period, from 20/11/23 to 31/05/24, covers the colder period of the year, during which indoor radon levels generally tend to be higher. Radon activity concentrations values are reported along with the uncertainties, as calculated with the GammaVision Software (GammaVision®). Uncertainty is calculated as the square root of quadrature summing of all individual uncertainties from the analysis, including counting uncertainty, nuclide uncertainty and efficiency uncertainty. A comprehensive description can be found in the software manual, available in (GammaVision®).

As reported in Table 2, the median of measured values is 363 Bq/m^3, the maximum reported value is 1164 ± 120 Bq/m^3, the minimum value is 87 ± 12 Bq/m^3, and the mean of the reported activity concentration values is 395 ± 210 Bq/m^3. This mean value exceeds the reference level of 300 Bq/m^3 indicated by current regulations.

Rather than the high mean value, susceptible to the influence of potential outliers, what is noteworthy is that results are homogeneous,

Table 2
Some statistical indicators on reported indoor radon concentration measurements.

Mean concentration across all measurements	395 Bq/m^3
Mean concentration in tuff buildings	417 Bq/m^3
Median	363 Bq/m^3
Minimum reported concentration	87 ± 12 Bq/m^3
Maximum reported concentration	1164 ± 120 Bq/m^3
% of measurements exceeding the reference level of 300 Bq/m^3 (Legislative Decree 1010/2020)	70 %
% of measurements not significantly different from the reference level of 300 Bq/m^3 (considering measurement uncertainty)	15 %
% of measurements below the reference level	8 %

Table 1
Results of radon gas concentrations for each room, floor, and time. The measurement uncertainty is expressed as expanded uncertainty with coverage factor $k = 2$ (95 % confidence interval). Tuff rooms in the basement are shown in green; tuff rooms on the ground floor are shown in blue; tuff rooms and the first floor are shown in yellow; and concrete rooms are shown in gray.

Intended use	Code	Building materials	Wall covering	Floor	Radon activity PERIOD I (Bq/m^3)	Radon activity PERIOD II (Bq/m^3)
Ecclesiastical structure I	S1	Tuff	Plaster	−1	542 ± 57	509 ± 53
Ecclesiastical structure I	T1	Tuff	Plaster	0	362 ± 40	390 ± 41
Ecclesiastical structure I	T2	Tuff	Plaster	0	182 ± 22	441 ± 43
Ecclesiastical structure II	S2	Tuff	Plaster	−1	378 ± 41	330 ± 35
Ecclesiastical structure II	S3	Tuff	Plaster	−1	402 ± 44	319 ± 34
Ecclesiastical structure II	P1	Tuff	Plaster	1	399 ± 43	376 ± 40
Ecclesiastical structure II	T3	Tuff	Plaster	0	251 ± 28	272 ± 29
Ecclesiastical structure II	P2	Tuff	Plaster	1	456 ± 49	461 ± 48
Private study	T4	Tuff	Plaster	0	363 ± 40	363 ± 39
Commercial activity	T5	Tuff	Plaster	0	467 ± 50	493 ± 52
Public office	T6	Tuff	Plaster	0	334 ± 37	346 ± 37
Commercial activity	T7	Tuff	Wood	0	558 ± 59	869 ± 89
Commercial activity	T8	Tuff	Plaster	0	87 ± 13	137 ± 16
Commercial activity	T9	Tuff	Tuff	0	345 ± 38	332 ± 36
Underground cavity	S4	Tuff	Tuff	−1	1164 ± 120	943 ± 97
Church	T10	Tuff	Plaster	0	297 ± 33	470 ± 49
Ecclesiastical structure III	T11	Tuff	Plaster	0	481 ± 51	391 ± 41
Ecclesiastical structure III	T12	Concrete	Plaster	0	142 ± 18	268 ± 29
Ecclesiastical structure III	T13	Tuff	Plaster	0	234 ± 27	298 ± 32
Ecclesiastical structure III	T14	Concrete	Pvc panels	0	87 ± 12	270 ± 29

with 70 % of the measurements exceeding 300 Bq/m^3 as shown in Fig. 2.

The high percentage of indoor environments with values exceeding 300 Bq/m^3 suggests that the municipality could be classified as a priority area for radon risk according to the PNAR (Currie, 1968). It would be sufficient for 15 % of 16 measurement points to exceed 300 Bq/m^3 to be classified as a priority area. This study found that about 70 % of the 20 measurement points exceeded the reference value. Detailed discussion of the results for each environment is reported in supplementary (2.S CR-39 Survey results discussion).

Indoor radon activity concentrations typically increase during winter (Di Carlo et al., 2023; Pulinets et al., 2024). This trend was observed in 13 of the 20 measurement points. While an inversion was noted in the remaining 7, the differences were small and within measurement error. This could be due to an exceptionally hot summer leading to increased use of air conditioning and a mild winter encouraging ventilation. However, the inversion in 3 measurement points within the same ecclesiastical structure, as well as in the tuff cellar (S4), may indicate that the buildup of indoor radon is predominantly attributed to the construction materials used rather than to the influx of radon from beneath the ground. Specifically, the diffusion of radon from BMs is enhanced under conditions of high temperature. Conversely, the accumulation of radon from subsurface sources is augmented by an increasing temperature gradient between the indoor and outdoor areas, particularly during winter months. Several studies reported that the seasonal trend reversal can be attributed to convective flows of radon-bearing air, which, through permeable soil, can reach indoor environments, especially those developed on elevated areas positioned on pyroclastic soil (Di Carlo et al., 2023; Moreno et al., 2024).

However, paired *t*-test has been performed to evaluate seasonal differences between radon period I (warmer months) and period II (colder period). The calculated p-values 0.1935 was found to be greater than the critical value of 0.05, indicating a lack of significance. There is no significant difference in radon concentrations during the two period of analysis; they remain closely similar to each other. This observation can be attributed to the well-known natural thermal insulation properties of the tuff

3.2. Results: gamma spectrometry

Gamma spectrometry analysis was conducted on three distinct types of tuffs from Sant'Agata de' Goti. Three samples were analyzed for each tuff type. The mean activity concentrations of Ra-226, Th-232, K-40, and used to calculate index *I*, as shown in Table 3. These results were then compared to previously reported values for similar types of tuffs in literature.

The measured specific activities of tuff samples align with literature values, supporting the classification of the material. Variations within the same tuff type might be attributed to distinct lithological zones at different sampling sites. The results indicate that the grey tuff from Sant'Agata de' Goti poses potential radiation protection concerns.

Table 3
Results of gamma spectroscopy measurements and calculation of *I* for both samples of this study (SADG) and samples of the same type in literature. * Indicates values calculated by authors.

	Ra-226 (Bq/kg)	Th-232 (Bq/kg)	K-40 (Bq/kg)	*I* index
SADG1	104 ± 10	190 ± 19	1301 ± 130	1.73
SADG2	105 ± 10	181 ± 18	1233 ± 123	1.66
Grey tuff (1) in (Nuccetelli et al., 2017)	79 ± 3	106 ± 6	1387 ± 52	1.26
Grey tuff (2) in (Nuccetelli et al., 2017)	90 ± 4	102 ± 6	1945 ± 70	1.46
Grey tuff (Tuoro-Caserta) in (Nuccetelli et al., 2017)	107 ± 4	121 ± 6	1740 ± 61	1.54*
Grey tuff in (Sabbarese et al., 2021)	85 ± 3	106 ± 6	1747 ± 61	1.39*
Grey tuff in (Nuccetelli et al., 2017)	243	542	1925	4.16

3.3. Results: exhalation

Table 4 shows the mean values of parameters useful for calculating exhalation and emanation of the three samples for each type of tuff, SADG1 and SADG2.

The duration of measurements and the radon background were the same in all cases. Similarly, volume and surface area were kept more or less constant for the two types of sample states (rock or powder). The variable parameters for each type of sample were radon activity concentration and mass.

Table 5 shows the results for η, R, R_m, R_s These values were compared with those documented in literature for similar types of grey tuffs from the Campania region (Sabbarese et al., 2021). The uncertainty of each value is about 10 %.

Radon emanation and exhalation from tuff are not solely determined by ^{226}Ra. Petrographic characteristics, such as grain size and porosity, also play a significant role. The high emanation/exhalation potential of the Sant'Agata de' Goti tuff, more than its high radionuclide levels, suggests a risk of elevated indoor radon levels. The high indoor radon concentrations observed in this study are likely attributed to the construction materials, in addition to the fluxes from the subsoil (Di Carlo et al., 2023).

Additionally, this research aimed to investigate whether the process of pulverizing construction materials influences their emanation and exhalation properties. Many measurement techniques require samples to be powdered, which, as our results indicate, can lead to an overestimation or underestimation of the actual radon emissions from these

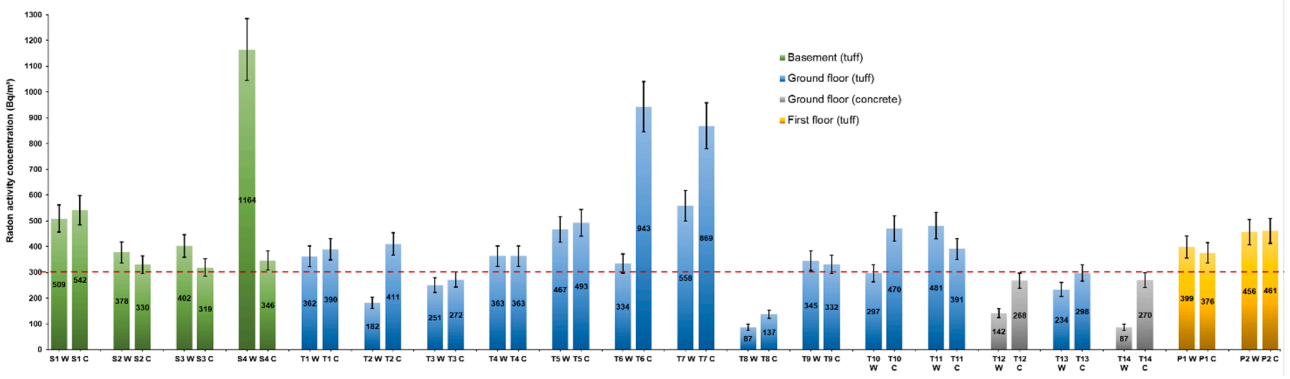

Fig. 2. Results of the individual measurements for each room and for each period - warm (W) and cold (C) - in relation to reference level of the legislation.

Table 4
Parameters of the measurements and physical characteristics of the samples.

	Duration of measurements (days)	Radon background (Bq/m^3)	Radon activity concentration (Bq/m^3)	Volume (m^3)	Surface area (m^2)	Mass (kg)
SADG1 rock	5	10	180	0.000077513	0.0148088	0.10324
SADG1 powder			210	0.000063478	0.00453416	0.07082
SADG1 rock			178	0.000077513	0.0148088	0.12324
SADG2 powder			215	0.000063478	0.00453416	0.07582

Table 5
Results of η, R, R_m, R_s calculation both samples of this study (SADG) and of samples of the same type in literature.

	η (%)	R (Bq/d)	R_m (Bq/(kg·h))	R_s (Bq/(m^2·h))
SADG1 (rock)	15	0.31	0.12	0.85
SADG1 (powder)	27	0.36	0.21	3.31
SADG2 (rock)	12	0.30	0.10	0.34
SADG2 (powder)	25	0.37	0.20	3.39
Grey tuff rock (1) in (*Jochum and Enzweiler, 2014*)	8	//	0.05	0.91
Grey tuff rock (2) in (*Jochum and Enzweiler, 2014*)	12	//	0.08	1.56

materials. The primary cause of this variation in values is attributed to the drastic change in porosity, although a change in grain moisture content, which significantly influences the emanation coefficient, may also contribute (Sakoda et al., 2010).

For all samples, exhalation and emanation parameters increase when transitioning from rock to powder, as expected (Zheng et al., 2024); notably, η and R_m increase by 72 %, and R_s by 285 % for SADG1 sample, whereas η and R_m increase by 99 %, and Rs by 300 % for SADG2.

3.4. Results: mineralogical, petrographic and porosimetry characterization

Mineralogical and petrographic characterizations were carried out on lithotypes (samples SADG1 and SADG2) that exhibiting similar features to those used in the construction of the historic buildings and shows radiometric anomalies. Petrographic analyses were performed on thin sections, whereas rock fragments were investigated for mineral morphological features and qualitative chemical composition using SEM-EDS. Bulk-rock quantitative chemical analyses were also carried out using XRF. Calcination was performed on the samples to determine their Loss on Ignition (LOI). It is important to note that the mineralogical characterization presented in this study is based on petrographic microscopy and SEM-EDS analyses. Although X-ray diffraction (XRD) is a widely employed technique for quantitative mineral identification, previous studies on the Campanian Ignimbrite facies have demonstrated that zeolitic phases (mainly phillipsite, with subordinate smectite), when restricted to small microdomains or vesicle infillings, frequently occur in concentrations below the typical XRD detection limit (≈3–5 wt %). This observation is consistent with our thin-section and SEM results,

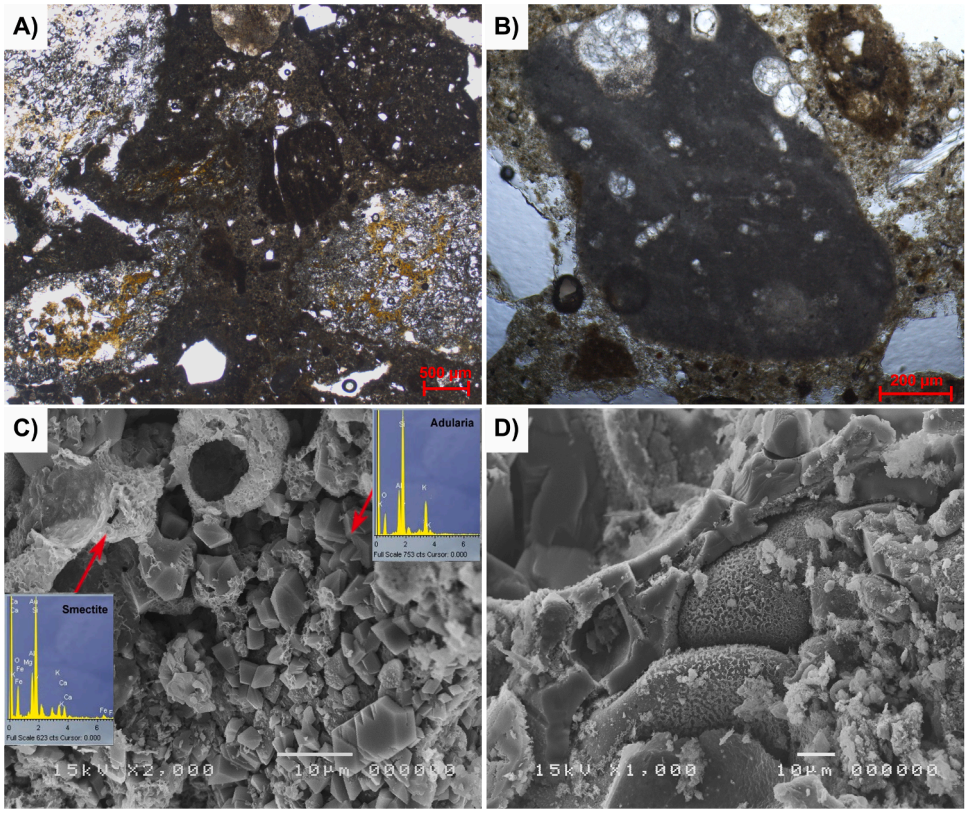

Fig. 3. A) Thin-section image under polarized light showing lithic fragments (pumiceous and carbonate) and the glassy matrix of the tuff; B) Thin-section image under polarized light illustrating carbonate lithic fragments containing visible planktonic foraminiferal shells; C) SEM micrograph of zeolitized pumice and/or glass displaying adularia crystals and smectite, as supported by qualitative SEM–EDS analyses; D) SEM micrograph showing vesicles and microfractures connecting pumiceous clasts.

which reveal a localized yet overall limited degree of zeolitization within pumice fragments. Consequently, XRD analysis would likely not significantly alter the qualitative mineralogical interpretation proposed here. Nonetheless, future work will include XRD analyses on an expanded dataset to further refine the quantitative relationship between secondary mineral phases and radon emanation behavior

The SADG1 sample is a greyish rock with relatively fine grain, containing scattered pumiceous, scoriaceous, and lithic lapilli. Studies conducted on thin sections reveal a dark pumiceous and scoriaceous lapilli, often rounded (Fig. 3A and B), along with fragments of feldspar and clinopyroxene crystals. Additionally, numerous lithic fragments of carbonate nature are observed, in which planktonic foraminifera shells are visible (Fig. 3B). Rarely, in some pumice cavities, philipsite and adularia crystals are found, as well as smectite, as identified by SEM-EDS analysis (Fig. 3C). Observations of microstructural features indicate a well-developed primary porosity, with vesicles and microfractures connecting pumiceous and scoriaceous clasts (Fig. 3D). These features suggest differences in pore connectivity across the sample, which could influence radon diffusion and emanation.

Chemically, XRF analyses (Table 6) show a high concentration of CaO and Sr, at 13.35 wt % and 1345 ppm respectively, with an unusually high LOI for this type of material (16.76 wt %). This is attributed to the significant presence of carbonate lithic fragments. Elevated concentrations of Th and U, at 92 ppm and 30 ppm respectively, are also noted (Table 6). Based on bibliographic data regarding geochemical, mineralogical, and petrographic descriptions, the sample could originate from the WGI-LYT transition zone (Langella et al., 2013; Scarpati et al., 2020; Pappalardo et al., 1999), although discrepancies remain in the Th and U contents found in the chemical analyses (Fedele et al., 2008; Arienzo et al., 2011; Belkin et al., 2016).

The SADG2 sample is a yellowish fine-grained rock with dispersed pumiceous and lithic lapilli. Studies conducted on thin sections reveal the presence of large pumice lapilli and smaller, darker scoriaceous and lithic fragments (Fig. 4a). Fragments of feldspar and clinopyroxene crystals are present. Moreover, elongated zeolite crystals, likely philipsite, are widespread and clearly visible within a pumice void (Fig. 4b and c). SEM-EDS analyses confirm the presence of philipsite crystals, which are often associated with an alteration patina of smectite and large fragments of sodium-rich plagioclase (albite, Fig. 4d). Microstructural observations of SADG2 indicate interconnected vesicles and primary porosity within pumice clasts, as well as microfractures that may facilitate gas transport. These qualitative observations provide insights into the potential pathways for radon diffusion. XRF analyses show a high concentration of CaO and Sr, at 12.15 wt % and 1589 ppm respectively; Na_2O levels are also significant (2.21 wt %). In this case as well, anomalous LOI values were detected. The high values of CaO and LOI are related to carbonate lithic fragments and zeolites (Langella et al., 2013); the higher levels of Na_2O are likely linked to the presence of Na-rich philipsite and large albite fragments (Fig. 4c and d). Chemical analyses also show elevated levels of Th and U (Fedele et al., 2008; Arienzo et al., 2011; Belkin et al., 2016), at 117 ppm and 18 ppm respectively (Table 6). Based on the mineral-petrographic description and geochemical analyses, the studied rock can be attributed to the lithified yellow tuff unit (Langella et al., 2013; Scarpati et al., 2020).

The mercury intrusion porosimetry (MIP) analysis performed on samples SADG1 and SADG2 provides quantitative evidence supporting the petrographic observations on vesicularity and microstructural connectivity. Both tuffs exhibit high total porosity, equal to 44.79 % for SADG1 and 46.97 % for SADG2, consistent with the widespread presence of primary vesicles and microfractures within pumice and scoriaceous clasts described in Campanian Ignimbrite facies (Langella et al., 2013; Scarpati et al., 2020; Allocca et al., 2022). Total pore volume values (0.338 and 0.363 cm^3/g for SADG1 and SADG2, respectively) align with the abundance of vesiculated pumice fragments observed in thin section and SEM analyses. The higher total pore surface area measured in SADG2 (6.785 m^2/g versus 4.908 m^2/g in SADG1) is consistent with its more pervasive zeolitization and the widespread presence of philipsite and smectite infillings (Cappelletti et al., 2003; Di Benedetto et al., 2015), which are known to increase the internal surface area of altered ignimbrites. Differences in average and modal pore diameters (SADG1: 0.276 μm and 1.883 μm; SADG2: 0.214 μm and 4.3 μm) reflect contrasting degrees of vesicle coalescence and secondary mineral overgrowth, in agreement with the variability reported for welded and lithified tuff facies (Scarpati et al., 2020). Overall, the porosimetric parameters strongly support mineralogical and petrographic observations, confirming that the studied tuffs possess a highly porous and microfractured framework characteristic of Campanian Ignimbrite materials (Cappelletti et al., 2003; Langella et al., 2013).Table 7

Table 6
Average chemical analyses of CI facies.

	SADG1	SADG2
SiO_2	53.02	53.20
TiO_2	0.57	0.58
Al_2O_3	16.26	16.17
Fe_2O_3	3.96	3.86
MnO	0.13	0.15
MgO	1.66	1.46
CaO	13.35	12.15
Na_2O	0.85	2.21
K_2O	9.88	9.96
P_2O_5	0.09	0.10
TOT	99.77	99.84
LOI*	16.76	16.39
Rb	360	409
Sr	1345	1587
Y	42	427
Zr	532	5807
Nb	38	42
Ba	817	974
Cr	27	5
Ni	26	22
Sc	11	5
V	152	76
Co	3	3
Cu	11	12
Zn	99	99
Ga	22	19
Hf	12	13
Ta	3	3
Pb	148	155
Th	92	117
U	30	18

4. Conclusion

The correlation between the different experimental methods enabled a synergistic data interpretation, strengthening the overall risk assessment. Radon concentration measurements obtained using CR-39 detectors revealed values exceeding the regulatory threshold in 70 % of the monitored sites (Kemski et al., 2012). These results are consistent with those obtained through E-PERM measurements, which confirmed a high exhalation capacity of the local tuff (Koumantakis et al., 2017). This suggests a clear relationship between the properties of the building materials and the accumulation of radon in indoor environments (Turhan et al., 2017). Furthermore, gamma spectrometry quantified high specific activities of Ra-226 and Th-232, in agreement with thorium and uranium concentrations determined via XRF (Chen et al., 2018). This supports the hypothesis that the materials studied represent a primary source of radon (Al-Harthy et al., 2016). Results of Th-232 have shown measured activity concentration values almost by a factor 2 times higher compared to Ra-226. This fact highlights the crucial contribution of Rn-220 to indoor radon, coming from building materials. Measuring and modeling Rn-220 exhalation could be crucial for assessing total indoor radiation risk, especially in areas with volcanic geology.Thorium and Uranium concentrations measured in the tuff

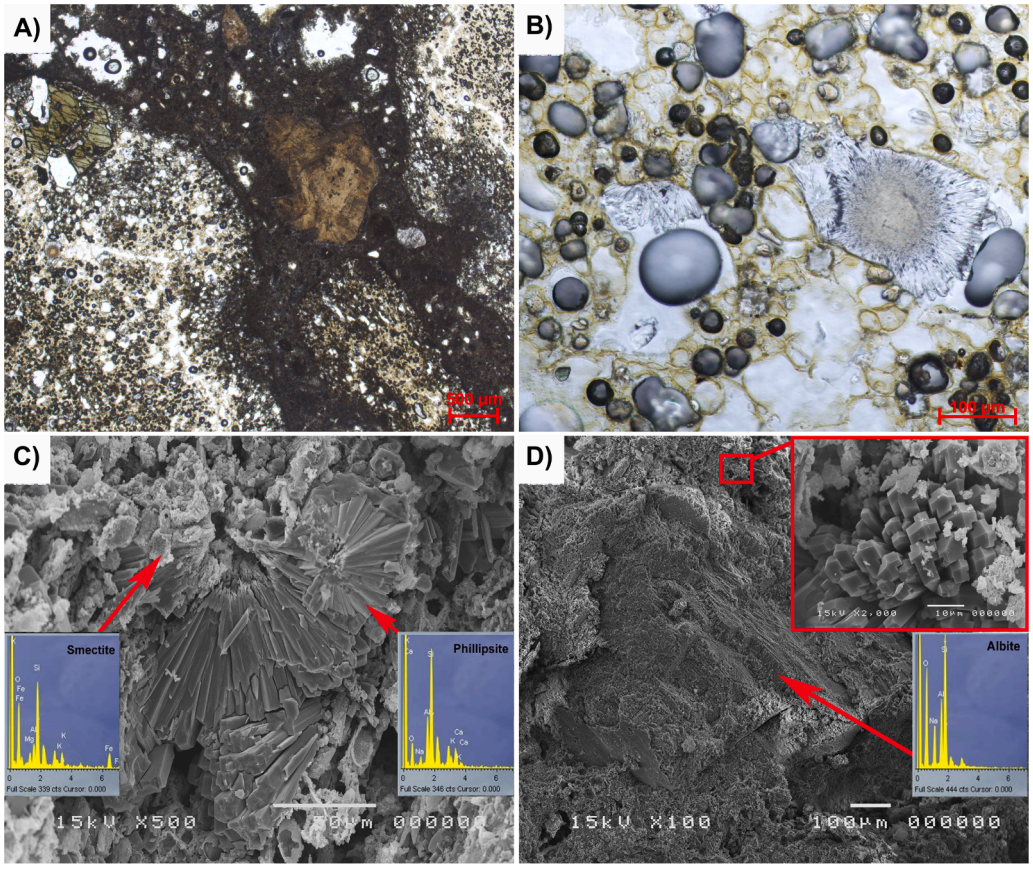

Fig. 4. A) Thin-section image under polarized light showing large pumice lapilli associated with smaller, darker scoriaceous and lithic fragments; B) Thin-section image under polarized light revealing abundant elongated zeolite crystals—likely phillipsite—clearly visible within a pumice vesicle; C) SEM micrograph showing large phillipsite crystals with Na-rich composition indicated by qualitative SEM–EDS analyses, along with smectite within pumice vesicles; D) SEM micrograph of large albite crystal fragments and phillipsite within vesicles (highlighted in yellow). Mineralogical identification is supported by qualitative SEM–EDS data.

Table 7
Porosity data of ignimbrites measured by mercury intrusion porosimetry (MIP).

	SADG1	SADG2
Total pore surface area (m^2/g)	4.908	6.785
Bulk density (g/cm^3)	1.3245	1.2946
Apparent density (g/cm^3)	2.3989	2.4415
Total pore volume (cm^3/g)	0.33813	0.36283
Average pore diameter (μm)	0.2756	0.2139
Modal pore diameter (μm)	1.883	4.3
Porosity by Hg intrusion (%)	44.79	46.97

samples are relatively high, and, on average, exceed the values commonly reported in literature for similar materials. Nevertheless, they are consistent with the Campanian Ignimbrite origin and the trachyphonolitic composition of the volcanic products, as documented in comparable facies (Langella et al., 2013; Arienzo et al., 2011). This is particularly true for zeolitized or altered facies, where uranium and thorium may be hosted in devitrified glassy matrices, secondary minerals such as smectite and phillipsite, or accessory phases (Arienzo et al., 2011; Belkin et al., 2016). Mineralogical and textural observations indicate that the studied tuffs possess well-developed primary porosity, vesicles, and microfractures, with zeolitic phases (phillipsite) and smectites filling some voids. These microstructural features suggest variations in pore connectivity and effective porosity, which can significantly influence radon diffusion and emanation. The data therefore indicate that microstructural and mineralogical characteristics may play a more important role in radon release than radionuclide concentration alone (Buzcu-Guven et al., 2014; Giusti et al., 2013). Anomalous behavior was observed in SADG2 (see section on Electret Ion Chamber), where pulverization led to a decrease, rather than an increase, in exhalation parameters. This phenomenon might be attributable to the higher LOI, as well as zeolitized pumices and fossiliferous carbonate clasts, which may reduce effective porosity and hinder radon transport in the powdered form (Kojima et al., 2011). The porosimetric results substantially reinforce the interpretation of radon behaviour by demonstrating the key role of microstructural features in controlling emanation and exhalation dynamics. High porosity values (≈45–47 %), together with connected pore networks in the micrometric range, create highly efficient pathways for radon transport, as already highlighted in studies linking ignimbrite vesicularity to gas mobility (Sakoda et al., 2010; Cappelletti et al., 2003). The higher pore surface area in SADG2 correlates with its more significant zeolitization, a process known to modify effective porosity and internal surface geometry (Langella et al., 2013), while the presence of secondary minerals such as philipsite and smectite may further influence radon retention and release (Arienzo et al., 2011; Belkin et al., 2016). These microstructural characteristics provide a mechanistic explanation for the elevated radon emanation coefficients observed in powdered samples and are consistent with the higher indoor radon concentrations detected in buildings constructed with these tuffs (Di Carlo et al., 2023; Turhan et al., 2017). The integration of petrographic, radiometric, and porosimetric data therefore confirms that the intrinsic physical fabric of the Campanian Ignimbrite—characterised by high vesicularity, microfracturing, and zeolite-rich alteration domains—plays a primary role in radon generation and mobility, often exerting a stronger influence than radionuclide content alone (Nuccetelli et al., 2020; Moreno et al., 2024). Finally, the *I* index exceeded the regulatory threshold in two of the analyzed tuff

types. This evidence, combined with the observed high exhalation potential, confirms the need to consider existing building materials in the planning of mitigation strategies outlined in the PNAR. The integration of the adopted analytical techniques thus enables the proposal of targeted mitigation interventions, grounded in quantitative and scientifically validated data. Despite the complexity of adopting remedial actions (Hodgson et al., 2011), which does not allow for an instant solution, increased passive ventilation (e.g., window opening times and openings to the outside) has been prescribed. The next step will be to conduct further radon gas monitoring to verify the effectiveness of this remedial action and, if not, proceed with the evaluation of structural interventions, consistent with legislative and/or regulatory constraints.

Funding sources

This research did not receive any specific grant from funding agencies in the public, commercial, or not-for-profit sectors.

CRediT authorship contribution statement

Fabrizio Ambrosino: Writing – review & editing, Visualization, Validation, Methodology, Investigation, Formal analysis, Data curation. **Manuela Rossi:** Writing – review & editing, Visualization, Validation, Methodology, Investigation, Formal analysis, Data curation. **Andrea D'Elia:** Writing – review & editing, Writing – original draft, Methodology, Formal analysis. **Chiara Imparato:** Writing – review & editing, Writing – original draft, Data curation. **Mariagabriella Pugliese:** Writing – review & editing, Visualization, Validation, Supervision, Resources, Project administration, Funding acquisition, Data curation, Conceptualization. **Giuseppe La Verde:** Writing – review & editing, Writing – original draft, Visualization, Validation, Supervision, Project administration, Methodology, Investigation, Conceptualization.

Declaration of competing interest

The authors declare the following financial interests/personal relationships which may be considered as potential competing interests:

Reports a relationship with that includes: Has patent pending to. If there are other authors, they declare that they have no known competing financial interests or personal relationships that could have appeared to influence the work reported in this paper.

Acknowledgments

The authors acknowledge Dr. Abner Colella (Department of Earth, Environmental and Resources Sciences) for his prompt availability in performing porosity measurements on the samples.

Supplementary materials

Supplementary material associated with this article can be found, in the online version, at doi:10.1016/j.hazadv.2026.101055.

Data availability

Data will be made available on request.

References

Al-Harthy, A., et al., 2016. Radon exhalation and uranium concentration in building materials used in Oman. Radiat. Phys. Chem. 120, 25–31. https://doi.org/10.1016/j.radphyschem.2015.11.019.

Allocca, V., et al., 2022. Hydraulic properties of ignimbrites: matrix and fracture permeabilities in two pyroclastic flow deposits from Cimino-Vico volcanoes (Italy). Bull. Eng. Geol. Environ. 81, 221. https://doi.org/10.1007/s10064-022-02712-0.

Ambrosino, F., et al., 2024. Radon exhalation rate: a metrological approach for radiation protection. Sensors 24 (11), 3633. https://doi.org/10.3390/s24113633.

Arienzo, I., et al., 2011. Processes and timescales of magma evolution prior to the campanian Ignimbrite eruption (Campi Flegrei, Italy). Earth. Planet. Sci. Lett. 306 (3–4), 217–228. https://doi.org/10.1016/j.epsl.2011.04.002.

Artiola, V., et al., 2021. Sassi of Matera building material: highresolution gammaray spectroscopy characterization for radioprotection. Buildings 11 (6), 258. https://doi.org/10.3390/buildings11060258.

Belkin, H.E., et al., 2016. Mineralogy and geochemistry of the older (>40ka) ignimbrites on the Campanian Plain, southern Italy. J. Volcanol. Geotherm. Res. 323, 1–18. https://doi.org/10.1016/j.jvolgeores.2016.05.002.

Buzcu-Guven, B., et al., 2014. Mineralogical controls on radon emanation and diffusion in volcanic tuff. Appl. Radiat. Isot. 88, 12–18. https://doi.org/10.1016/j.apradiso.2014.01.003.

Cappelletti, P., et al., 2003. Post-eruptive processes in the Campanian Ignimbrite. Mineral. Petrol. 79, 79–97. https://doi.org/10.1007/s00710-003-0003-7.

Carannante, G., et al., 2011. Note Illustrative della Carta Geologica D'italia Alla Scala 1: 50 000 Foglio 431 (Caserta Est). Servizio Geologico d'Italia (ISPRA), Rome, Italy.

Chao, C.Y.H., Tung, T.C.W., 1999. Radon emanation of building material—impact of back diffusion and difference between one-dimensional and three-dimensional tests. Health Phys. 76, 675–681. https://hdl.handle.net/1783.1/25292.

Chen, J., et al., 2018. Assessment of natural radionuclide concentrations in building materials using gamma spectrometry and XRF. J. Environ. Radioact. 182, 94–101. https://doi.org/10.1016/j.jenvrad.2017.12.013.

Chiocchini, U., et al., 2009. Carta Geologica d'Italia - Foglio 432 - Benevento, scala 1: 50.000. Progetto CARG – ISPRA.

European Commission, 2002. Radiation Protection 122: Practical Use of the Concepts of Clearance and Exemption – Part II: Guidance on General Clearance Levels For Practices. Office for Official Publications of the European Communities, Luxembourg.

Council Directive 2013/59/Euratom of 5 December 2013, 2014. Laying down basic safety standards for protection against the dangers arising from exposure to ionising radiation, and repealing directives 89/618/Euratom, 90/641/Euratom, 96/29/Euratom, 97/43/Euratom and 2003/122/Euratom. Off. J. Eur. Union L13, 1–73.

Currie, L.A., 1968. Limits for qualitative detection and quantitative determination. Application to radiochemistry. Anal. Chem. 40 (3), 586–593. https://doi.org/10.1021/ac60259a007.

Darby, S., et al., 2005. Radon in homes and risk of lung cancer: collaborative analysis of individual data from 13 European case-control studies. BMJ 330, 223. https://doi.org/10.1136/bmj.38308.477650.63.

de Jong, P., et al., 2005. Interlaboratory comparison of three methods for the determination of the radon exhalation rate of building materials. Health Phys. 88 (1), 59–64. https://doi.org/10.1097/01.hp.0000144573.53642.d9.

De Vivo, B., et al., 2001. New constraints on the pyroclastic eruptive history of the Campanian volcanic Plain (Italy). Mineral. Petrol. 73, 47–65. https://doi.org/10.1007/s007100170010.

Decreto Legislativo 26 maggio 2000, n. 241, 2000. Attuazione della direttiva 96/29/Euratom in materia di protezione sanitaria della popolazione e dei lavoratori contro i rischi derivanti dalle radiazioni ionizzanti. Gazzetta Ufficiale Serie Generale n.203 del 31-08-(Suppl. Ordinario n. 138).

Decreto Legislativo 31 luglio 2020, n. 101. Attuazione della direttiva 2013/59/Euratom, che stabilisce norme fondamentali di sicurezza relative alla protezione contro i pericoli derivanti dall'esposizione alle radiazioni ionizzanti, e che abroga le direttive 89/618/Euratom, 90/641/Euratom, 96/29/Euratom, 97/43/Euratom e 2003/122/Euratom e riordino della normativa di settore in attuazione dell'articolo 20, comma 1, lettera a), della legge 4 ottobre 2019, n. 117. Gazzetta Ufficiale Serie Generale n.201 del 12-08-2020 (Suppl. Ordinario n. 29).

Di Benedetto, C., et al., 2015. Porosity as key factor in the durability of two historical building stones: Neapolitan Yellow Tuff and Vicenza Stone. Eng. Geol. 193, 310–319. https://doi.org/10.1016/j.enggeo.2015.05.006.

Di Carlo, C., et al., 2023. Extreme reverse seasonal variations of indoor radon concentration and possible implications on some measurement protocols and remedial strategies. Environ. Pollut. 327, 121480. https://doi.org/10.1016/j.envpol.2023.121480.

Di Girolamo, P., Rolandi, G., Stanzione, E.D., 1973. L'eruzione di pomici a letto dell'Ignimbrite Campana. Period Miner. 42, 436–468.

European Union, 2011. Regulation 305/2011, 2011 of the European Parliament and of the Council of 9 March 2011 laying down harmonised conditions for the marketing of construction products and repealing Council Directive 89/106/EEC, 2011. Off. J. Eur. Union 88. L4 April.

Fedele, L., et al., 2008. The Breccia Museo formation, Campi Flegrei, southern Italy: geochronology, chemostratigraphy and relationship with the Campanian Ignimbrite eruption. Bull. Volcanol. 70, 1189–1219. https://doi.org/10.1007/s00445-008-0197-y.

Fews, A.P., Henshaw, D.L., 1982. High resolution alpha particle spectroscopy using CR-39 plastic track detector. Nucl. Instrum. Methods Phys. Res. A 197 (2–3), 517–529. https://doi.org/10.1016/0167-5087(82)90349-0.

GammaVision® Maestro-PRO® Gamma-Ray Spectrum Analysis and MCA emulators for Microsoft® Windows® 7, 8.1, and 10 professional manual Available from: https://www.ortec-online.com/-/media/ametekortec/manuals/a/a66-mnl.pdf?la=en&revision=dd63bfec-f5cd-4579-8201-e81a52f7fb78.

Giusti, A., et al., 2013. Influence of microstructure and mineralogy on radon exhalation from natural stones. J. Environ. Radioact. 120, 1–6. https://doi.org/10.1016/j.jenvrad.2013.02.014.

Hodgson, S.A., et al., 2011. An analysis of radon remediation methods." reports of health protection agency–centre for radiation. Chem. Environ. Hazard, Chilton, Didcot, Oxfordshire.

International Agency for Research on Cancer (IARC), 2012. IARC Monographs on the Evaluation of Carcinogenic Risks to Humans: A Review of Human Carcinogens – Chemical Agents and Related Occupations, 100F. IARC, Lyon, pp. 73–82.
International Commission on Radiological Protection (ICRP), 2014. Radiological protection against radon exposure. ICRP Publication 126. Ann. ICRP 43 (3).
ISO 15901-1:2016 Evaluation of pore size distribution and porosity of solid materials by mercury porosimetry and gas adsorption — Part 1: mercury porosimetry.
ISTAT. Demo Popolazione e Statistiche. 2025 [accessed 2025 Jul 27]. Available from: https://demo.istat.it/app/?i=POS&l=it.
Jochum, K.P., Enzweiler, J., 2014. Reference materials in geochemical and environmental research. editors. In: Holland, H.D., Turekian, K.K. (Eds.), Treatise On Geochemistry, 2nd Edition. Elsevier, pp. 43–70. https://doi.org/10.1016/B978-0-08-095975-7.01403-0.
Kemski, J., et al., 2012. Mapping of natural radiation in the European Union. J. Environ. Radioact. 113, 33–41. https://doi.org/10.1016/j.jenvrad.2011.10.006.
Kojima, H., et al., 2011. Effect of powdering on radon emanation from volcanic tuff samples. Radiat. Meas. 46 (12), 1421–1425. https://doi.org/10.1016/j.radmeas.2011.09.003.
Kotrappa, P., Stieff, L.R., 1994. Application of NIST 222Rn emanation standards for calibrating 222Rn monitors. Radiat. Prot. Dosim. 55, 211–218.
Kotrappa, P., Stieff, F., 2009. Radon exhalation rates from building materials using electret ion chamber radon monitors in accumulators. Health Phys. https://doi.org/10.1097/HP.0b013e3181a9ab15.
Koumantakis, J., et al., 2017. Evaluation of radon exhalation from building materials by electret ion chambers and CR-39 detectors. Radiat. Prot. Dosim. 173 (3), 292–298. https://doi.org/10.1093/rpd/ncx089.
Krisiuk, E.M., et al., 1971. A Study of Radioactivity of Building Materials. Research Institute for Radiation Hygiene, Leningrad.
La Verde, G., et al., 2020. Radioactivity content in natural stones used as building materials in Puglia region analysed by high resolution gamma-ray spectroscopy: preliminary results. Constr. Build. Mater. 239, 117668. https://doi.org/10.1016/j.conbuildmat.2019.117668.
La Verde, G., et al., 2021. Gamma index in a typical building material of Ciglio area (Ischia Island). Solid State Phenomena 319, 24–29. https://doi.org/10.4028/www.scientific.net/SSP.319.24.
Langella, A., et al., 2013. New insights into the mineralogical facies distribution of Campanian Ignimbrite, a relevant Italian industrial material. Appl. Clay. Sci. 72, 55–73. https://doi.org/10.1016/j.clay.2013.01.008.
Liu, Y., et al., 2024. Radon and lung cancer: current status and future prospects. Crit. Rev. Oncol./Hematol. 198, 104363. https://doi.org/10.1016/j.critrevonc.2024.104363.
Markkanen, M., 1995. Report STUK-B-STO 32. Radiation and Nuclear Safety Authority-STUK.
Martell, M., et al., 2023. Evaluation of radon action plans: searching for a systematic and standardised method. Int. J. Environ. Res. Public Health 20, 7128. https://doi.org/10.3390/ijerph20237128.
Ministero della Salute, 2024. Piano nazionale d'azione per il radon 2023-2032. Supplemento ordinario n. 10 alla Gazzetta Ufficiale Serie Generale n 43, 21 febbraio.
Monti, L., et al., 2011. Carta Geologica d'Italia - Foglio 431 - Caserta Est, scala 1:50.000. Progetto CARG – ISPRA.
Moreno, P., et al., 2024. Comparative analysis of techniques for estimating radon exhalation from building materials. Radiat. Phys. Chem. 222, 111866. https://doi.org/10.1016/j.radphyschem.2024.111866.
National Research Council, 2006. Biological Effects of Ionizing Radiation (BEIR) VII: Health Risks from Exposure to Low Levels of Ionizing Radiation, Phase 1. National Academies Press, Washington, DC.
Nuccetelli, C., et al., 2017. Natural Radioactivity in Building Materials in the European Union: a Database of Activity concentrations, Radon Emanations and Radon Exhalation Rates. Istituto Superiore di Sanità, Roma. Rapporti ISTISAN 17/36.
Nuccetelli, C., et al., 2020. Building material radon emanation and exhalation rate: need of a shared measurement protocol from the European database analysis. J. Environ. Radioact. https://doi.org/10.1016/j.jenvrad.2020.106438.
Pappalardo, L., et al., 1999. Chemical and Sr-isotopical evolution of the Phlegraean magmatic system before the Campanian Ignimbrite and the Neapolitan Yellow Tuff eruptions. J. Volcanol. Geotherm. Res. 91 (2–4), 141–166. https://doi.org/10.1016/S0377-0273(99)00033-5.
Pawel, D.J., Puskin, J.S., 2004. The U.S. Environmental Protection Agency's assessment of risks from indoor radon. Health Phys. 87, 68–74. https://doi.org/10.1097/00004032-200407000-00008.
Petropoulos, N.P., et al., 2001. Building materials radon exhalation rate: ERRICCA intercomparison exercise results. Sci. Total. Environ. 272 (1–3), 109–118. https://doi.org/10.1016/S0048-9697(01)00674-X.
Poffijn, A., et al., 1984. Laboratory measurements of radon exhalation and diffusion. Radiat. Prot. Dosim. 7, 77–79. https://doi.org/10.1093/rpd/7.1-4.77.
Pugliese, M., et al., 2024. Preliminary spectrometric analysis measurements of the Sant'Agata De' Goti Tuff in the framework of the National Radon Action Plan. In: 2024 IEEE International Workshop on Metrology for Living Environment (MetroLivEnv). Chania, Greece, pp. 302–306. https://doi.org/10.1109/MetroLivEnv60384.2024.10615658.
Pulinets, S., et al., 2024. Radon variability as a result of interaction with the environment. Atmosphere 15 (2), 167. https://doi.org/10.3390/atmos15020167.
Rad Elec Inc, 2024. E-PERM® System User's Manual. Version 4.0.1. March 11. https://device.report/rad-elec.
Righi, S., Bruzzi, L., 2006. Natural radioactivity and radon exhalation in building materials used in Italian dwellings. J. Environ. Radioact. 88 (2), 158–170. https://doi.org/10.1016/j.jenvrad.2006.01.009.
Sabbarese, C., et al., 2020. Analysis by scanner of tracks produced by radon alpha particles in CR-39 detectors. Radiat. Prot. Dosim. 191 (2), 154–159. https://doi.org/10.1093/rpd/ncaa140.
Sabbarese, C., et al., 2021. Radiological characterization of natural building materials from the Campania region (Southern Italy). Const. Bldg. Mat. 268, 121087. https://doi.org/10.1016/j.conbuildmat.2020.121087.
Sakoda, A., et al., 2010. Experimental and modeling studies of grain size and moisture content effects on radon emanation. Radiat. Meas. 45 (2), 204–210. https://doi.org/10.1016/j.radmeas.2010.01.010.
Scarpati, C., et al., 2020. Dynamics of large pyroclastic currents inferred by the internal architecture of the Campanian Ignimbrite. Sci. Rep. 10, 22230. https://doi.org/10.1038/s41598-020-79164-7.
Scotto di Santolo, A., et al., 2014. Preservation of cultural heritage of Sant'Agata De'Goti (Italy) from natural hazards. Engineering Geology for Society and Territory-Volume 8: Preservation of Cultural Heritage. Springer International Publishing, Cham, pp. 421–425. https://doi.org/10.1007/978-3-319-09408-3_73.
Silva, A.S., de, Lurdes, Dinis, M., et al., 2022. An overview of the development and implementation of the radon action plans in European countries. In: Arezes, P.M., et al. (Eds.), Occupational and Environmental Safety and Health III. Studies in Systems, Decision and Control, Occupational and Environmental Safety and Health III. Studies in Systems, Decision and Control, 406. Springer, Cham, pp. 203–211. https://doi.org/10.1007/978-3-030-89617-1_21.
Turhan, S., et al., 2017. Relationship between building materials properties and indoor radon concentrations. J. Environ. Radioact. 169-170, 99–105. https://doi.org/10.1016/j.jenvrad.2016.11.004.
UNI EN ISO 11665-7:2015, 2012. Measurement of radioactivity in the environment — Air: radon-222 — Part 7: accumulation method for estimating surface exhalation rate. Int. Organ. Stand.
UNI EN ISO 18589-2:2015, 2015. Measurement of Radioactivity in the Environment - Soil - Part 2 Guidance for the Selection of the Sampling strategy, Sampling and Pretreatment of Samples. ISO, Geneva, Switzerland.
UNI ISO 11665-4:2020, 2020. Measurement of Radioactivity in the Environment – Radon-222 – Part 4: Continuous measurement Method of the Activity Concentration. Ente Nazionale Italiano di Unificazione.
UNI ISO 11665-9:2019, 2019. Measurement of radioactivity in the environment — Air: radon-222 — Part 9: test methods for exhalation rate of building materials. Int. Organ. Stand.
UNSCEAR, 2000. Sources and Effects of Ionizing Radiation, I. United Nations Scientific Committee on the Effects of Atomic Radiation, New York.
UNSCEAR, 2008. Sources and effects of ionizing radiation. Report to the General Assembly, With Scientific Annexes. United Nations Scientific Committee on the Effects of Atomic Radiation, New York.
UNSCEAR. Sources, 2012. Effects and risks of ionizing radiation. Report to the General Assembly, With Scientific Annexes (A and B). United Nations, New York.
World Health Organization (WHO), 2009. Global Health Risks: Mortality and Burden of Disease Attributable to Selected Major Risks. WHO, Geneva.
Zheng, X., et al., 2024. Effect of hygroscopicity of typical powder solid wastes on their radon exhalation characteristics. Sci. Total. Environ. 944, 173956. https://doi.org/10.1016/j.scitotenv.2024.173956.